

NexusGS: Sparse View Synthesis with Epipolar Depth Priors in 3D Gaussian Splatting

Yulong Zheng¹, Zicheng Jiang¹, Shengfeng He², Yandu Sun¹, Junyu Dong¹, Huaidong Zhang³, Yong Du^{1*}

¹ Ocean University of China,

² Singapore Management University, ³ South China University of Technology

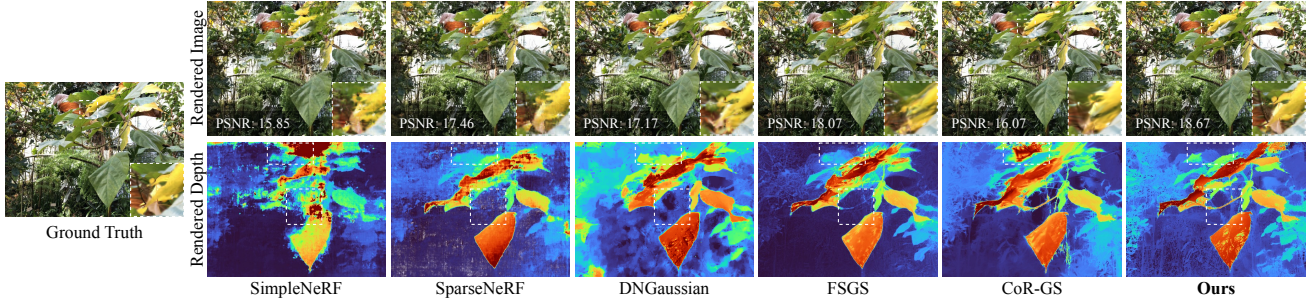


Figure 1. NexusGS distinguishes itself from both NeRF-based and 3DGS-based competitors by incorporating epipolar depth priors, significantly improving the accuracy of depth maps and enhancing the fidelity of rendered images. This effectiveness in handling sparse input views is achieved through innovative point cloud densification with depth blending and pruning strategies.

Abstract

Neural Radiance Field (NeRF) and 3D Gaussian Splatting (3DGS) have noticeably advanced photo-realistic novel view synthesis using images from densely spaced camera viewpoints. However, these methods struggle in few-shot scenarios due to limited supervision. In this paper, we present NexusGS, a 3DGS-based approach that enhances novel view synthesis from sparse-view images by directly embedding depth information into point clouds, without relying on complex manual regularizations. Exploiting the inherent epipolar geometry of 3DGS, our method introduces a novel point cloud densification strategy that initializes 3DGS with a dense point cloud, reducing randomness in point placement while preventing over-smoothing and overfitting. Specifically, NexusGS comprises three key steps: Epipolar Depth Nexus, Flow-Resilient Depth Blending, and Flow-Filtered Depth Pruning. These steps leverage optical flow and camera poses to compute accurate depth maps, while mitigating the inaccuracies often associated with optical flow. By incorporating epipolar depth priors, NexusGS ensures reliable dense point cloud coverage and supports stable 3DGS training under sparse-view conditions. Experiments demonstrate that NexusGS significantly enhances depth accuracy and rendering quality, surpassing state-of-the-art methods by a considerable margin. Furthermore, we validate the

superiority of our generated point clouds by substantially boosting the performance of competing methods. Project page: <https://usmizuki.github.io/NexusGS/>.

1. Introduction

Neural Radiance Field (NeRF) [23] and 3D Gaussian Splatting (3DGS) [19] have recently advanced the field of photo-realistic novel view synthesis by leveraging images captured from densely spaced camera viewpoints to reconstruct 3D scenes under supervised conditions. However, these methods exhibit limitations in few-shot scenarios due to the reduced availability of supervision. Consequently, recent research has focused on improving the generalization of NeRF and 3DGS models in sparse-view settings to enhance their applicability in real-world contexts such as virtual reality and augmented reality.

Sparse view synthesis methods based on NeRF [42, 45] typically rely on backpropagation combined with additional priors and regularization strategies to guide the learning of implicit radiance fields. Despite their progress, they inherit a key limitation of NeRF: the need for random sampling during volumetric rendering along each ray, which results in high training and rendering costs. While subsequent acceleration techniques [1, 2, 38, 46] face a trade-off between computational expense and rendering quality.

*Corresponding author (csyongdu@ouc.edu.cn).

In contrast, 3DGS uses Gaussian primitives to model 3D geometry from sparse point clouds, typically generated by Structure-from-Motion (SfM) [32], and offers a more efficient solution with its splat-based rasterization, enabling real-time, high-quality rendering. However, the application of 3DGS in sparse view synthesis is less explored compared to NeRF-based methods. A major challenge lies in densifying the initial point clouds to ensure comprehensive scene coverage with limited data, which depends critically on two factors: the number of points and their positional accuracy.

In 3DGS, the number of points is increased through a split operation during adaptive density control. In dense-view novel view synthesis, rich supervision effectively reduces randomness in point placement. However, this method struggles in sparse-view scenarios due to the lack of constraints, leading to oversmoothed reconstructions and poor generalization. FSGS [51] addresses this by introducing a Gaussian Unpooling mechanism, which generates new Gaussians at the centers of edges connecting a prototype Gaussian to its K -nearest neighbors. Nevertheless, this approach often results in point clustering, neglecting areas between clusters and hindering the formation of a reliable dense point cloud.

On the other hand, improving the positional accuracy of 3D points often requires incorporating additional geometric priors. Depth information serves as a crucial link between 2D imagery and 3D reconstruction, with many methods [20, 42, 51] leveraging depth maps predicted by monocular estimators [3, 28, 29]. These approaches typically impose depth-aware regularizations to address the scale ambiguity inherent in monocular perception. However, these handcrafted constraints often prove inadequate, as they lack explicit metric grounding and merely redistribute rather than eliminate scale errors.

In this paper, we introduce NexusGS, a 3DGS-based method for novel view synthesis from limited-view images. Our approach embeds depth information into point clouds to leverage the epipolar representation capabilities of 3DGS, enabling accurate geometric modeling without the need for complex manual regularization. The core of our method is a point cloud densification technique. Unlike traditional methods that gradually densify point clouds through split operations, our approach aims to form a relatively dense point cloud at the initial stage, reducing placement randomness and alleviating oversmoothing or overfitting in sparse view synthesis. This technique comprises three key steps: Epipolar Depth Nexus, Flow-Resilient Depth Blending, and Flow-Filtered Depth Pruning.

Drawing inspiration from triangulation, the Epipolar Depth Nexus step uses optical flow and camera poses within an epipolar geometry framework to compute depth accurately and explicitly. Given that optical flow estimates can be inaccurate, leading to inconsistent depth maps, we propose Flow-Resilient Depth Blending, which selects depths with

minimal sensitivity to flow errors by evaluating the relative rate of change between reference and projection distances. Flow-Filtered Depth Pruning further refines the depth maps by removing points that are too far from the epipolar line, thus mitigating the impact of optical flow inaccuracies.

Although optical flow predictions may be imprecise, they tend to be more stable than depth maps due to their image-resolution-bound solution space. In contrast, depth maps span an unbounded domain, with errors propagating through scene-dependent scales, causing error bounds to grow linearly with the depth range. By leveraging optical flow for epipolar depth computation and incorporating our proposed strategies, NexusGS achieves reliable initial dense point cloud coverage. This foundation supports stable 3DGS training under sparse-view conditions, resulting in highly accurate depth maps and improved image quality (see Fig. 1).

In summary, the contributions of this work are threefold:

- We enhance sparse view synthesis by embedding epipolar depth priors into 3DGS, avoiding errors from monocular depth estimations and bypassing complex regularizations.
- We present a point cloud densification technique for 3DGS that ensures accurate depth computation from sparse inputs using optical flow and camera poses, mitigates the impact of flow prediction inaccuracies, and delivers reliable dense point cloud coverage.
- Extensive experiments demonstrate that NexusGS outperforms state-of-the-art methods in both depth accuracy and rendering quality across a variety of scenes, including real-world and object-centric scenarios. Furthermore, the superiority of our generated point clouds is validated by significantly enhancing the performance of competing methods.

2. Related Work

Radiance Fields. Neural Radiance Fields (NeRFs) have revolutionized 3D scene reconstruction and novel view synthesis by utilizing neural representations via volumetric rendering. While NeRF produces high-quality images, its computational intensity leads to slow training and inference times. To address this, various techniques have been developed to improve efficiency [12, 24, 30, 38], along with methods focused on enhancing image quality [6, 13, 37, 41] and generalization capabilities [18, 39, 43, 47]. Complementing these efforts, 3D Gaussian Splatting (3DGS) [7, 14, 19, 48] offers an explicit alternative, using anisotropic 3D Gaussians for fast, high-quality, real-time rendering. As an explicit method, 3DGS excels in capturing fine details in complex scenes and continues to emerge as a robust approach alongside implicit methods like NeRF.

Sparse View Synthesis Using NeRF. Synthesizing novel views from sparse input images is a critical yet challenging task in computer vision. Traditional NeRF models [1, 44], which heavily rely on extensive data, struggle in sparse-view scenarios due to their dependence on dense input for accu-

rate reconstruction. Recent research [33, 45, 47, 50] has sought to mitigate these challenges by incorporating various regularization techniques, such as depth supervision to improve training efficiency and reduce the number of required views [10], geometry regularization to stabilize the learning process [25, 36], and semantic constraints using high-dimensional spaces like CLIP [11, 15, 27].

As a core element of sparse-view synthesis, acquiring and leveraging depth priors effectively has become a key focus in the field. For example, early work such as DS-NeRF [9] introduces a sparse depth prior to constrain the scene reconstruction process, while DDP-NeRF [31] further enriches this prior by explicitly modeling uncertainty, making it more comprehensive but less reliable. Simple-RF [35] proposes filtering out depth priors using image self-information but fails to obtain a dense depth prior without relying on reliable depth maps. In contrast, SCADE [40] combines monocular depth estimates to obtain a better depth prior, yet this prior is learned through probabilistic optimization, making it uncertain and still sparse or unreliable.

In summary, most of these methods can only acquire sparse depth priors or unreliable dense priors due to inadequately suited regularizations. Moreover, NeRF’s reliance on volume rendering continues to pose challenges, particularly in balancing rendering speed with image quality.

Sparse View Synthesis Using 3DGS. In contrast to the flourishing development of NeRF-based sparse view synthesis methods, the application of 3D Gaussian Splatting (3DGS) in sparse-view scenarios has encountered difficulties in maintaining consistent reconstructions with minimal input. Emerging methods, such as DR-3DGS [8], and FSGS [51], attempt to address these issues through depth-based constraints or point cloud densification techniques. CoR-GS [49] trains and jointly refines multiple 3DGS fields simultaneously, constraining point cloud generation. CoherentGS [26] enforces pixel-Gaussian binding to suppress densification noise at the cost of constrained primitive counts. Despite these efforts, these approaches often suffer from inaccuracies arising from depth estimations, failing to adequately model the relationship between monocular depth estimates and true depth, underscoring the necessity for more robust strategies to improve 3DGS performance in sparse-view contexts. Our work builds on these foundations by proposing a novel co-regularization framework that overcomes the limitations of existing methods. Specifically, we focus on enhancing the consistency of Gaussian radiance fields in sparse-view scenarios using epipolar depth priors, moving beyond the reliance on monocular depth maps, avoiding the manual design of complex regularizations, and pushing the boundaries of sparse-view novel view synthesis.

We also recognize an additional class of sparse-view synthesis methods based on multi-view stereo (MVS), such as MVSNeRF [5], PixelSplat [4], and MVSGaussian [21].

However, these methods rely on large datasets and require dense image inputs from the same scene for training to achieve high reconstruction quality, which falls outside the scope of this paper. In contrast, our approach operates within the constraints of sparse training images and does not require extensive pre-training, enabling us to attain high-quality reconstructions with minimal data requirements.

3. Preliminaries

Gaussian Splatting. 3D Gaussian Splatting [19] depicts 3D scenes using a set of Gaussians $G(\cdot)$, each defined as:

$$G(x) = e^{-\frac{1}{2}(x-\mu)^\top \Sigma^{-1}(x-\mu)}, \quad (1)$$

where x denotes a point in 3D space, and μ represent the center of the 3D Gaussian. The covariance matrix Σ can be decomposed as $\Sigma = RSS^\top R^\top$, where $R \in \mathbb{R}^{3 \times 3}$ is a rotation matrix, and $S \in \mathbb{R}^{3 \times 1}$ are the scale parameters. Each Gaussian also includes spherical harmonics (SH) coefficients for color $c \in \mathbb{R}^{3 \times 1}$, and an opacity value.

For pixel rendering, 3DGS sorts the 3D Gaussian primitives intersecting a pixel’s camera ray. Let Q be the ordered set of Gaussians along the ray, with i representing the index of each element in Q . The renderer computes the color c_i and opacity α_i for each Gaussian, *i.e.*, $\{\alpha_i, c_i \mid i \in Q\}$, and determines the pixel color as follows:

$$C = \sum_{i \in Q} c_i \alpha_i \prod_{j=1}^{i-1} (1 - \alpha_j), \quad (2)$$

where the summation represents the accumulated color, and the product accounts for the cumulative transmittance.

During training, 3DGS initializes with a sparse point cloud and uses L1 and D-SSIM losses between the rendered and ground truth images to guide the optimization process.

Epipolar Line. As shown on the left side of Fig. 2, for a point p_i in the source view i , the corresponding epipolar line l_{p_i} in the target view j can be determined as follows:

$$(a, b, c)^\top = F^{i \rightarrow j}(x_i, y_i, 1)^\top, \quad (3)$$

where $F^{i \rightarrow j}$ is the fundamental matrix from the source camera to the target camera, and (x_i, y_i) represents the coordinate of point p_i in the source image. The epipolar line equation in the target camera’s pixel coordinate system is then given by:

$$ax + by + c = 0. \quad (4)$$

4. Approach

Epipolar Depth Nexus. A major challenge in 3DGS when applied to sparse-view novel view synthesis arises from the randomness introduced by the split operation during adaptive density control, combined with the limited supervision from

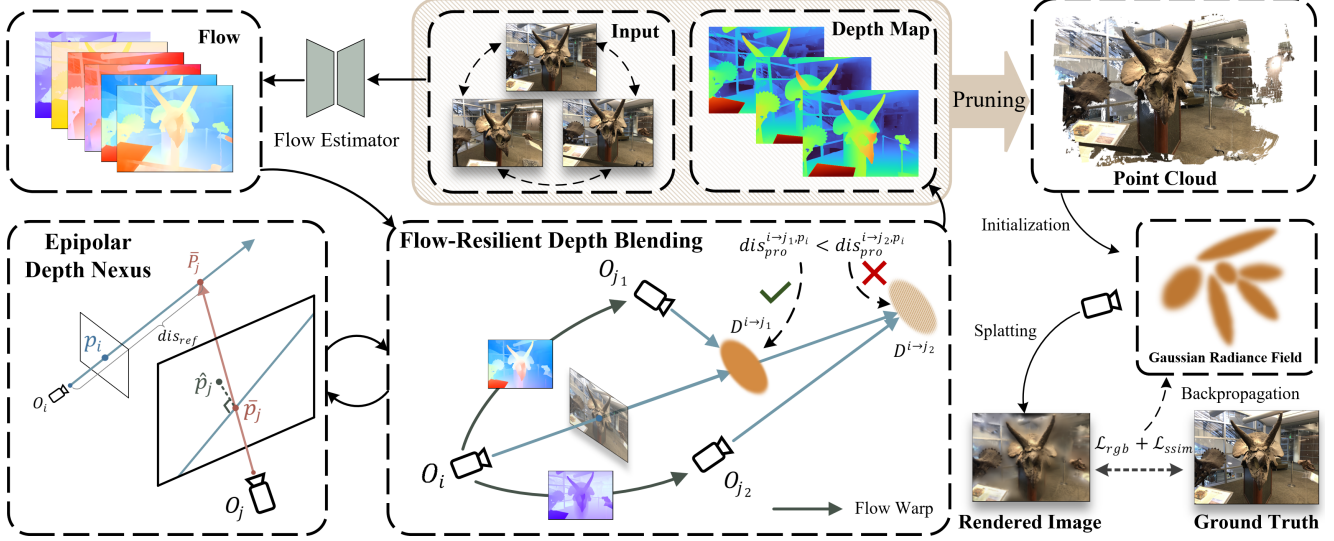


Figure 2. Given a few input images, our method first computes depth using optical flow and camera poses at the Epipolar Depth Nexus step. We then fuse depth values from different views, minimizing flow errors with flow-resilient depth blending. Before forming the final dense point cloud, outlier depths are removed at the flow-filter depth pruning step. In training, we do not need depth regularization, thanks to the embedded epipolar depth prior in the point cloud.

sparse training data. To overcome this, NexusGS proposes initializing with a dense point cloud, as shown in the pipeline in Fig. 2.

Each point in the point cloud used for 3DGS has at least two key attributes: color and position. While input images can guide the color assignment, they cannot provide accurate depth values, which are crucial for determining the precise positions of the points. Monocular depth estimation networks often fail to deliver reliable depth information. In contrast, our approach overcomes this by establishing a nexus between the epipolar line and depth, using optical flow and camera parameters to compute accurate depth values.

To begin with, we predict optical flow between views using existing optical flow estimators [34] as follows:

$$M_{flow}^{i \rightarrow j} = f(I_i, I_j), \quad (5)$$

where $f(\cdot)$ denotes the pre-trained flow estimator, I_i and I_j are the given images of the source and target views, respectively. For a point p_i in the source view, the predicted matched point \hat{p}_j in the target view is given by:

$$\hat{p}_j = p_i + M_{flow}^{i \rightarrow j}(p_i). \quad (6)$$

The true matched point p_j should ideally lie on the epipolar line l_{p_i} in the target view. However, due to estimation errors, the predicted point \hat{p}_j from the flow estimator often deviates from this condition. To mitigate this, we relax \hat{p}_j by selecting the perpendicular foot \bar{p}_j on the epipolar line l_{p_i} , which is the closet point to \hat{p}_j . The computation is as follows:

$$\bar{p}_j = \left(\frac{b^2 \hat{x}_j - ab \hat{y}_j - ac}{a^2 + b^2}, \frac{a^2 \hat{y}_j - ab \hat{x}_j - bc}{a^2 + b^2} \right), \quad (7)$$

where (\hat{x}_j, \hat{y}_j) are the coordinates of point \hat{p}_j in the camera coordinate system, $\{a, b, c\}$ are the parameters of the epipolar line from Eq. (4). With \bar{p}_j , we can explicitly compute the depth value of p_i using epipolar geometry:

$$D^{i \rightarrow j}(p_i, \bar{p}_j) = \frac{|H \times -(R_i R_j^{-1} T_j - T_i)|}{|(K_i^{-1}(x_i, y_i, 1)^\top) \times H|}, \quad (8)$$

$$\text{where } H = (R_j R_i^{-1})^{-1} K_j^{-1}(\bar{x}_j, \bar{y}_j, 1)^\top.$$

Here, \times denotes the cross product, and R_i, T_i, R_j, T_j are the extrinsic parameters, while K_i and K_j are the intrinsic parameters of the source and target cameras.

Flow-Resilient Depth Blending. Given a limited number N of input images $\{I_i | i = 1, 2, \dots, N\}$, for a pixel p_i in a source view image I_i , we can identify the corresponding $N-1$ matched points $\{\hat{p}_j | j = 1, 2, \dots, i-1, i+1, \dots, N\}$ in the other $N-1$ views and compute the corresponding $N-1$ depth values using Eq. (8) with the point \bar{p}_j , which is a relaxation of \hat{p}_j . Although \bar{p}_j lies on the epipolar line, there can still be a distance error between it and the latent true matched point p_j . Since this error varies in magnitude across different views, it is necessary to effectively blend these depth values to produce the most accurate depth map.

A straightforward approach is to average the $N-1$ depth values. However, as shown in Fig. 3 (a), this method is sensitive to errors and often leads to greater deviations from the true 3D corresponding point P compared to selecting the depth value closest to P . Nevertheless, since the exact position of P is unknown, reliably identifying the depth value that best matches the true 3D location remains challenging.

We propose a flow-resilient depth blending strategy to address this issue. First, we define a reference distance

Method	LLFF (3 Views)				DTU (3 Views)				MipNeRF-360 (24 Views)			
	PSNR↑	SSIM↑	LPIPS↓	AVGE↓	PSNR↑	SSIM↑	LPIPS↓	AVGE↓	PSNR↑	SSIM↑	LPIPS↓	AVGE↓
Mip-NeRF [2]	14.62	0.351	0.495	0.240	8.68	0.571	0.353	0.315	21.23	0.613	0.351	0.118
DietNeRF [15]	14.94	0.370	0.496	0.233	11.85	0.633	0.314	0.232	20.21	0.557	0.387	0.135
RegNeRF [25]	19.08	0.587	0.336	0.139	18.89	0.745	0.190	0.107	22.19	0.643	0.335	0.107
FreeNeRF [45]	19.63	0.612	0.308	0.128	19.92	0.787	0.182	0.095	22.78	0.689	0.323	0.098
SparseNeRF [42]	19.86	0.624	0.328	0.128	19.55	0.769	0.201	0.102	22.85	0.693	0.315	0.097
DS-NeRF [9]	19.34	0.596	0.295	0.130	16.29	0.559	0.451	0.192	14.58	0.311	0.692	0.271
ViP-NeRF [36]	18.50	0.528	0.321	0.146	10.20	0.301	0.363	0.307	14.78	0.300	0.774	0.278
SimpleNeRF [35]	18.82	0.587	0.274	0.132	11.94	0.387	0.286	0.243	10.82	0.142	0.880	0.407
3DGS [19]	18.54	0.588	0.272	0.135	17.65	0.816	0.146	0.102	21.71	0.672	0.248	0.099
DNGaussian [20]	19.12	0.591	0.294	0.132	18.91	0.790	0.176	0.101	18.06	0.423	0.584	0.191
FSGS [51]	20.43	0.682	0.248	0.108	17.14	0.818	0.162	0.110	23.40	0.733	0.238	0.083
CoR-GS [49]	20.45	0.712	0.196	0.098	19.21	0.853	0.119	0.082	23.55	0.727	0.226	0.080
Ours	21.07	0.738	0.177	0.089	20.21	0.869	0.102	0.071	23.86	0.753	0.206	0.075

Table 1. Quantitative evaluations on the LLFF, DTU and Mip-NeRF360 datasets. For DNGaussian and FSGS training on DTU, we initialize with random point clouds when COLMAP fails due to sparse input images. The **best**, **second best**, and **third best** results are color-coded in each cell.

Thanks to the dense and accurate initial point cloud with epipolar depth priors, our approach does not require additional depth regularization in the objective function.

5. Experiments

5.1. Experimental Settings

Datasets. We evaluate our method on the LLFF [22], Blender [23], DTU [16], and Mip-NeRF360 [2] datasets, using the same splits and resolution as previous works [20, 25, 42, 45, 51]. Among these, LLFF is a real-world dataset focused on forward-facing scenes, Mip-NeRF360 is a large-scale dataset for 360-degree scenes, and DTU and Blender focus on object-centric datasets. For DTU, we apply masks to remove background influence, following prior methods [25]. Camera parameters are assumed to be known, consistent with other sparse view synthesis approaches [20, 49, 51].

Competitors. We compare our method against state-of-the-art approaches, including eight NeRF-based methods, such as SparseNeRF [42], DS-NeRF [9], ViP-NeRF [36], and SimpleNeRF [35], as well as recent 3DGS-based methods like DNGaussian [20], FSGS [51], CoR-GS [49], and the standard 3DGS [19]. Unless noted otherwise, all reported results are either taken from the original papers or obtained by training using the official code and default settings.

Metrics. Consistent with previous methods [20, 25, 42, 45, 49, 51], we use PSNR, SSIM, and LPIPS as evaluation metrics. Additionally, we compute the AVGE metric [25], which is the geometric mean of PSNR, SSIM, and LPIPS.

5.2. Comparison with State-of-the-Art Methods

LLFF. We summarize the quantitative results in Tab. 1. Our method outperforms all others in PSNR, SSIM, LPIPS, and AVGE on the LLFF dataset, achieving significant improvements of 0.62, 0.026, 0.019, and 0.009, respectively, over the second-best method.

Fig. 4 shows the visual comparisons, where our approach excels in both geometry and texture reconstruction. NeRF-based methods like ViP-NeRF struggle with geometry due to the lack of depth priors, as seen in the poor shape reconstruction. SimpleNeRF, using filtered depth priors, achieves better geometry but suffers from sparse depth, leading to incomplete reconstructions, especially at object edges. While DNGaussian and FSGS capture more texture detail, they are hindered by geometric inaccuracies from unreliable monocular depth maps, resulting in missing Gaussians and incomplete object reconstructions. Although CoR-GS has relatively complete depth maps, the overall reconstruction remains overly smooth and fails to capture high-frequency texture details. In contrast, our method, leveraging a dense and accurate point cloud with epipolar depth priors, not only reconstructs the full geometry but also captures finer details more effectively than the other methods.

MipNeRF-360. In the large-scale MipNeRF-360 dataset, obtaining accurate and dense point clouds under sparse-view settings is more challenging. Qualitative results are shown in Fig. 5. DNGaussian, being fast and lightweight, struggles with unbounded scenes. NeRF-based methods using depth priors, such as SimpleNeRF and ViP-NeRF, suffer from unreliable and sparse depth. Other 3DGS methods like FSGS and CoR-GS, while achieving good scores, still exhibit over-smoothing in large-scale scenes due to insufficient point cloud density. This demonstrates that initializing with sparse point clouds under limited supervision is inadequate for densification. In contrast, directly generating dense point clouds enables more complete scene reconstruction and finer details. As shown in Tab. 1, our method achieves state-of-the-art results across all metrics.

DTU. In this dataset, our visual comparisons, shown in Fig. 6, focus on comparing NexusGS with other 3DGS-based methods. Our reconstructed point cloud is denser and more

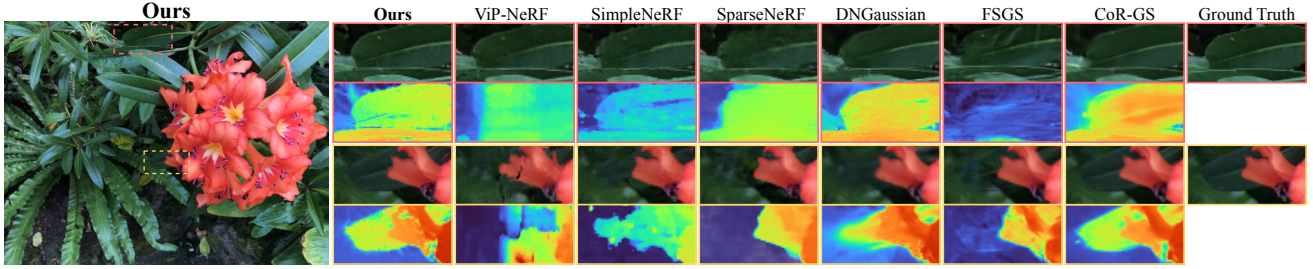


Figure 4. Visual comparisons on LLFF (3 views). Our method produces richer details and more accurate depth than all competitors.

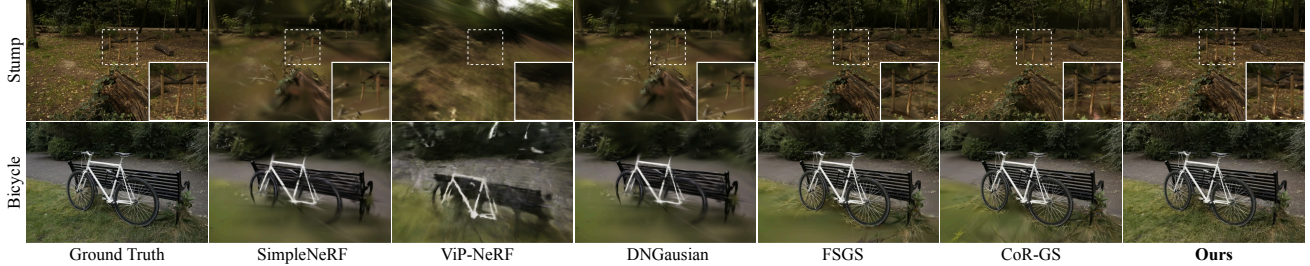


Figure 5. Visual comparisons on MipNeRF-360 (24 views). In large-scale scenes, NexusGS preserve detailed textures while others struggle.

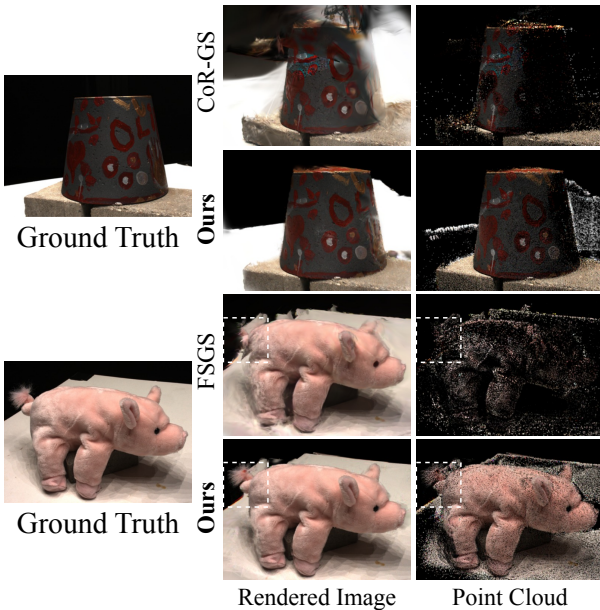


Figure 6. Visual comparisons on the DTU dataset (3 views). Our method produces a more comprehensive point cloud than others, resulting in higher-quality renderings.

accurate than those of CoR-GS and FSGS, which use the original 3DGS densification process and produce sparse or incomplete clouds. NexusGS also delivers superior rendering quality in terms of detail and texture. This highlights the effectiveness of initializing with a dense point cloud, rather than densifying from sparse views. Quantitative results can be found in Tab. 1, with additional visual comparisons in the supplementary materials.

Blender. We achieve state-of-the-art quantitative results on this dataset (Tab. 2). Despite the synthetic nature and lower

Method	Blender (8 Views)			
	PSNR \uparrow	SSIM \uparrow	LPIPS \downarrow	AVGE \downarrow
NeRF [23]	14.93	0.687	0.318	0.179
Simplified NeRF [15]	20.09	0.822	0.179	0.090
DietNeRF [15]	23.15	0.866	0.109	0.058
DietNeRF + ft [15]	23.59	0.874	0.097	0.053
FreeNeRF [45]	24.26	0.883	0.098	0.050
SparseNeRF [42]	22.41	0.861	0.119	0.063
3DGS [19]	22.23	0.858	0.114	0.064
FSGS [51]	22.70	0.822	0.137	0.068
CoR-GS [49]	23.98	0.891	0.094	0.050
DNGaussian [20]	24.07	0.885	0.090	0.049
Ours	24.37	0.893	0.087	0.047

Table 2. Quantitative evaluations on the Blender dataset.

demands for fine details, our method outperforms previous NeRFs, thanks to effective depth prior integration. While DNGaussian yields good results, it lacks the density of our point cloud. Additionally, CoR-GS suffers from degraded performance due to the absence of depth priors, whereas FSGS struggles to integrate them effectively, relying on a relaxed Pearson coefficient loss. Qualitative results are provided in the supplementary materials.

5.3. Ablation Study

We conduct ablation experiments on LLFF dataset with 3 views to assess the impact of Flow-Resilient Depth Blending (FRDB) and Flow-Filtered Depth Pruning (FFDP). We compare four depth blending strategies: Strategy **A** uses a simple average, **B** uses the depth from the nearest target view, and **C** employs a weighted average based on the inverse epipolar distance. FRDB (**D**) outperforms all others, providing superior reconstruction quality. Tab. 3 shows that applying FFDP further improves all strategies.

	Setting	PSNR \uparrow	SSIM \uparrow	LPIPS \downarrow	AVGE \downarrow
3DGS	/	18.54	0.588	0.272	13.469
Ours	A. Average	20.39	0.722	0.186	9.642
	B. Nearest	20.62	0.735	0.178	9.261
	C. Weighted Average	20.59	0.732	0.180	9.335
	D. FRDB	20.90	0.734	0.180	9.104
	E. Average + FFDP	20.51	0.725	0.184	9.502
	F. Nearest + FFDP	20.79	0.734	0.178	9.147
	G. Weighted + FFDP	20.78	0.735	0.178	9.148
	H. FRDB + FFDP	21.07	0.738	0.177	8.913

Table 3. Ablation study on LLFF with 3 training views. To clarify the comparison, the AVGE values are multiplied by $1e2$.

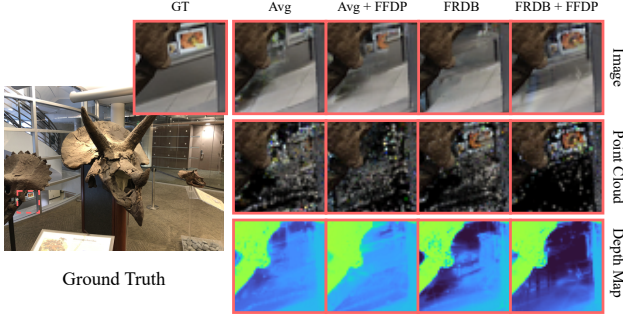


Figure 7. Visualization of ablation study results using 3-views.

In Fig. 7, we compare two representative strategies, **A** (Average) and **D** (FRDB). The mean strategy produces reasonable reconstructions but introduces errors in finer details, as seen in the point cloud, where erroneous points obscure the correct ones. During sparse-view training, these errors cannot be filtered out, leading to incorrect renderings. In contrast, FRDB with FFDP yields more accurate depth and a cleaner point cloud, significantly enhancing reconstruction. A comparison of depth maps highlights our method’s superior depth accuracy.

6. Generalizability Analysis

To evaluate the generalizability of the depth maps and initial point clouds generated by NexusGS, we integrate them into existing methods and assess their performance on the LLFF dataset, with results summarized in Tab. 4.

First, incorporating our depth maps as depth priors into SparseNeRF [42] yields significant improvements, showing their effectiveness in enhancing NeRF-based methods.

For 3DGS-based methods, both our depth maps and point clouds are effective. Applying either to DNGaussian [20] lead to notable improvements, similar to the gains seen with SparseNeRF. Compared to using fused stereo point clouds (DNGaussian*), our point clouds improve SSIM and LPIPS more than PSNR, likely due to DNGaussian’s reliance on inaccurate monocular depth maps for regularization. Nonetheless, our dense point clouds reduce over-smoothing, improving perceptual scores. Using only our depth maps improves PSNR, but DNGaussian’s point clouds still lack sufficient density, which may result in some over-smoothing. When both depth maps and point clouds are used together, or when

Method (3 views)	PSNR \uparrow	SSIM \uparrow	LPIPS \downarrow
SparseNeRF	19.86	0.624	0.328
SparseNeRF + Our Depth	20.23	0.647	0.313
DNGaussian	19.12	0.591	0.294
DNGaussian*	19.96	0.684	0.232
DNGaussian + Our Point Cloud (PC)	19.97	0.713	0.210
DNGaussian + Our Depth	20.09	0.694	0.220
DNGaussian + Our PC&Depth	20.11	0.723	0.200
DNGaussian w/o Depth + Our PC	20.10	0.719	0.202
FSGS	20.43	0.682	0.248
FSGS + Our PC	20.85	0.746	0.166
CoR-GS	20.45	0.712	0.196
CoR-GS + Our PC	21.00	0.744	0.176

Table 4. Versality of the depth map and initialized point cloud from our method. The best result for each method is highlighted in bold.

point clouds are used without depth loss, the depth information is better leveraged, resulting in improved SSIM and LPIPS scores. These configurations yield similar results, as the point clouds are derived directly from the depth maps.

For FSGS [51], which requires depth regularization on pseudo-views, we cannot apply our depth maps due to the difficulty in generating pseudo-view depths. However, using only our point clouds still yields significant improvements, further demonstrating the generalizability of our approach.

CoR-GS [49] optimizes two 3DGS radiance fields with co-regularization, constraining their rendering results with pseudo-views. Replacing the initial point cloud of one radiance field with ours leads to substantial improvement. The priors from our point cloud transfer effectively, combining the benefits of both the fused stereo point cloud and our dense point cloud. These results highlight the broad applicability and effectiveness of our method.

7. Conclusion

This paper presents NexusGS, a method that enhances sparse view synthesis in 3D Gaussian Splatting by embedding epipolar depth priors. Our approach uses optical flow and camera poses to compute accurate depth, yielding a reliable initial dense point cloud that improves rendering fidelity. Key components include Epipolar Depth Nexus for precise depth calculation, Flow-Resilient Depth Blending to reduce flow-induced errors, and Flow-Filtered Depth Pruning to eliminate inconsistent points. Experiments show that NexusGS outperforms state-of-the-art methods in depth accuracy and rendering quality, demonstrating the effectiveness of integrating epipolar depth information in sparse-view 3DGS.

Acknowledgements. This work is supported by the National Natural Science Foundation of China (No. 62102381, 41927805); Shandong Natural Science Foundation (No. ZR2021QF035); the National Key R&D Program of China (No. 2022ZD0117201); the Guangdong Natural Science Funds for Distinguished Young Scholar (No. 2023B1515020097); the AI Singapore Programme under the National Research Foundation Singapore (Grant AISG3-GV-2023-011); and the Lee Kong Chian Fellowships.

NexusGS: Sparse View Synthesis with Epipolar Depth Priors in 3D Gaussian Splatting

Supplementary Material

8. Derivations

8.1. Epipolar Depth Nexus

Once the coordinates of the perpendicular foot, denoted as \bar{p}_j , are determined in the target view's camera coordinate system (as shown in Eq. (7) in the main paper), the depth of point p_i , denoted as $D^{i \rightarrow j}(p_i, \bar{p}_j)$, can be computed using Eq. (8). Below, we provide a detailed derivation of Eq. (8) as presented in the main paper.

Since both p_i and \bar{p}_j are expressed in their respective camera coordinate systems, we first convert them into normalized image coordinates to facilitate the depth calculation. These coordinates, situated in their respective 3D domains, are referenced with the source view camera O_i and the target view camera O_j as origins. The transformation is formulated as follows:

$$\tilde{p}_i = K_i^{-1}(x_i, y_i, 1)^\top, \quad \tilde{p}_j = K_j^{-1}(\bar{x}_j, \bar{y}_j, 1)^\top, \quad (15)$$

where K_i and K_j represent the intrinsic parameters of the source and target cameras, while $(x_i, y_i), (\bar{x}_j, \bar{y}_j)$ are the image coordinates of points p_i and \bar{p}_j , respectively.

Next, we refer to Fig. 8 to elucidate the geometric relationships employed in our method. Notably, the triangles $\triangle O_i A \bar{P}_j$ and $\triangle O_i B \tilde{p}_i$ are similar, allowing us to establish the following relationship:

$$\frac{|\overrightarrow{O_i \bar{P}_j}|}{|\overrightarrow{O_i \tilde{p}_i}|} = \frac{|O_i A|}{|O_i B|} = \frac{D^{i \rightarrow j}(p_i)}{1}. \quad (16)$$

Here, $|\overrightarrow{O_i \bar{P}_j}|$ and $|\overrightarrow{O_i \tilde{p}_i}|$ represent the magnitudes of the respective vectors. Similarly, $|O_i A|$ and $|O_i B|$ represent the respective distances from O_i to the planes containing \bar{P}_j and \tilde{p}_i along the optical axis.

To further analyze the geometry, we introduce an auxiliary point \tilde{p}_i' such that $\overrightarrow{O_j \tilde{p}_i'}$ has the same length and direction as $\overrightarrow{O_i \tilde{p}_i}$. Projecting O_i perpendicularly onto the line $O_j \bar{P}_j$ yields point Q , and projecting \tilde{p}_i' onto the same line yields point U . The alternate interior angles $\angle O_i \bar{P}_j Q$ and $\angle \tilde{p}_i' O_j U$ are equal, leading to similar triangles $\triangle O_i \bar{P}_j Q$ and $\triangle \tilde{p}_i' O_j U$. Notice that triangles $\triangle O_i \tilde{p}_j O_j$ and $\triangle \tilde{p}_i' O_j \tilde{p}_j$ share the same base, allowing us to further derive Eq. (16) as follows:

$$D^{i \rightarrow j}(p_i) = \frac{|\overrightarrow{O_i \bar{P}_j}|}{|\overrightarrow{O_i \tilde{p}_i}|} = \frac{|O_i Q|}{|\tilde{p}_i' U|} = \frac{\text{Area}(\triangle O_i \tilde{p}_j O_j)}{\text{Area}(\triangle \tilde{p}_i' O_j \tilde{p}_j)}. \quad (17)$$

Using the formula for the area of a triangle, the above equation simplifies to:

$$D^{i \rightarrow j}(p_i) = \frac{|\overrightarrow{O_j \tilde{p}_j} \times \overrightarrow{O_j O_i}|}{|\overrightarrow{O_j \tilde{p}_i} \times \overrightarrow{O_j \tilde{p}_j}|}. \quad (18)$$

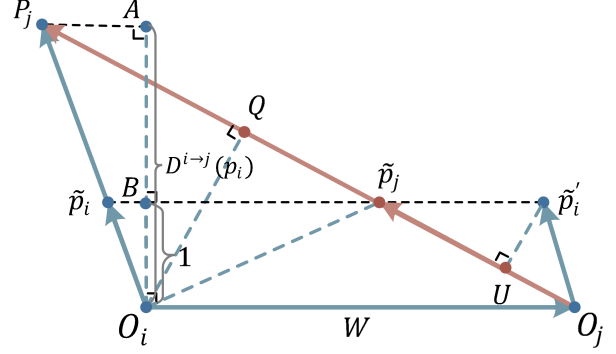


Figure 8. Illustration of the geometry relationships used in Epipolar Depth Nexus step.

The 3D coordinates of vectors $\overrightarrow{O_j \tilde{p}_j}$, $\overrightarrow{O_j O_i}$, and $\overrightarrow{O_j \tilde{p}_i}$ can be determined using the extrinsic parameter transformation formulas:

$$\begin{aligned} \overrightarrow{O_j \tilde{p}_j} &= \overrightarrow{O_i \tilde{p}_j} - \overrightarrow{O_i O_j} \\ &= (R_j R_i^{-1})^{-1} \tilde{p}_j + W - W \\ &= (R_j R_i^{-1})^{-1} K_j^{-1}(\bar{x}_j, \bar{y}_j, 1)^\top, \end{aligned} \quad (19)$$

$$\overrightarrow{O_j O_i} = -W = -(R_i R_j^{-1} T_j - T_i), \quad (20)$$

$$\overrightarrow{O_j \tilde{p}_i} = \overrightarrow{O_i \tilde{p}_i} = \tilde{p}_i, \quad (21)$$

where R_i, T_i and R_j, T_j are the extrinsic parameters of the source and target cameras. Finally, we plug Eqs. (19), (20) and (21) into Eq. (18) to obtain the analytical form of the depth of point p_i as follows:

$$D^{i \rightarrow j}(p_i) = \frac{|H \times -(R_i R_j^{-1} T_j - T_i)|}{|(K_i^{-1}(x_i, y_i, 1)^\top) \times H|}, \quad (22)$$

where $H = (R_j R_i^{-1})^{-1} K_j^{-1}(\bar{x}_j, \bar{y}_j, 1)^\top$.

8.2. Flow-Resilient Depth Blending

Here, we derive Eq. (9) from the main paper, used in our Flow-Resilient Depth Blending technique. Fig. 9 illustrates the geometric definitions of all relevant symbols. Our objective is to obtain the analytical form of the derivative of dis_{ref} with respect to dis_{pro} , denoted as $dis'_{ref}(dis_{pro}) = \frac{d dis_{ref}}{d dis_{pro}}$. This derivative is decomposed into two factors, $\frac{d dis_{ref}}{d \alpha}$ and $\frac{d \alpha}{d dis_{pro}}$, connected by the chain rule.

Derivation of $\frac{d dis_{ref}}{d \alpha}$. We begin by determining the expression of $\frac{d dis_{ref}}{d \alpha}$. Using the law of cosines and the law of sines, and referring to Fig. 9 (a) (similar to Fig. 3 (b) in the main paper), we

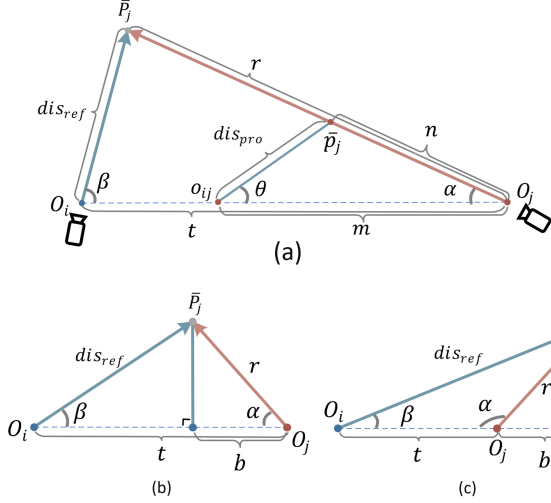


Figure 9. Illustration of the geometric definitions used.

derive the following equations:

$$\cos \beta = \frac{dis_{ref}^2 + t^2 - r^2}{2dis_{ref}t}, \quad (23)$$

$$r = \frac{dis_{ref} \sin \beta}{\sin \alpha}. \quad (24)$$

Substituting Eq. (24) into Eq. (23) and simplifying yields:

$$\begin{aligned} \frac{dis_{ref}^2 \sin^2 \beta}{\sin^2 \alpha} &= dis_{ref}^2 + t^2 - 2dis_{ref}t \cos \beta \\ &= dis_{ref}^2 \sin^2 \beta + dis_{ref}^2 \cos^2 \beta \\ &\quad + t^2 - 2dis_{ref}t \cos \beta \\ &= dis_{ref}^2 \sin^2 \beta + (dis_{ref} \cos \beta - t)^2. \end{aligned} \quad (25)$$

Furthermore, we rewrite Eq. (25) in the following form:

$$\begin{aligned} (dis_{ref} \cos \beta - t)^2 &= dis_{ref}^2 \sin^2 \beta \left(\frac{1}{\sin^2 \alpha} - 1 \right) \\ &= \frac{dis_{ref}^2 \sin^2 \beta \cos^2 \alpha}{\sin^2 \alpha}. \end{aligned} \quad (26)$$

Next, we isolate $\frac{\cos^2 \alpha}{\sin^2 \alpha}$ from the right-hand side of Eq. (26) to get:

$$\frac{\cos^2 \alpha}{\sin^2 \alpha} = \left(\frac{\cos \beta}{\sin \beta} - \frac{t}{dis_{ref} \sin \beta} \right)^2. \quad (27)$$

To take the square root of both sides of the equation, we need to ascertain the positive or negative nature of each side under the square root. Specifically, the formula after taking the square root can be determined based on geometric relationships. When $\frac{\cos \alpha}{\sin \alpha} > 0$, indicating that α is an acute angle, as illustrated in Fig. 9 (b), the following formulations hold:

$$\frac{\cos \beta}{\sin \beta} = \frac{t - b}{dis_{ref} \sin \beta}, \quad (28)$$

$$\frac{\cos \beta}{\sin \beta} - \frac{t}{dis_{ref} \sin \beta} = -\frac{b}{dis_{ref} \sin \beta} < 0, \text{ s.t. } \frac{\cos \alpha}{\sin \alpha} > 0. \quad (29)$$

Conversely, when $\frac{\cos \alpha}{\sin \alpha} < 0$, indicating that α is an obtuse angle, as illustrated in Fig. 9 (c), the following relationships hold:

$$\frac{\cos \beta}{\sin \beta} = \frac{t + b}{dis_{ref} \sin \beta}, \quad (30)$$

$$\frac{\cos \beta}{\sin \beta} - \frac{t}{dis_{ref} \sin \beta} = \frac{b}{dis_{ref} \sin \beta} > 0, \text{ s.t. } \frac{\cos \alpha}{\sin \alpha} < 0. \quad (31)$$

Combining both cases, we derive the following equation:

$$\frac{\cos \alpha}{\sin \alpha} = \frac{t}{dis_{ref} \sin \beta} - \frac{\cos \beta}{\sin \beta}, \quad (32)$$

and we can rewritten the above equation as follows:

$$dis_{ref} = \frac{t \sin \alpha}{\sin(\alpha + \beta)}. \quad (33)$$

Thus, we obtain the gradient expression of dis_{ref} with respect to α , which is formulated as follows:

$$\frac{ddis_{ref}}{d\alpha} = \frac{t \sin \beta}{\sin^2(\alpha + \beta)}. \quad (34)$$

Derivation of $\frac{d\alpha}{ddis_{pro}}$. Using a similar approach as for Eq. (33), we can derive the relationship between α and dis_{pro} :

$$dis_{pro} = \frac{m \sin \alpha}{\sin(\alpha + \theta)}. \quad (35)$$

Differentiating both sides with respect to dis_{pro} , we obtain $\frac{d\alpha}{ddis_{pro}}$, which are formulated as follows:

$$1 = \frac{m \cos \alpha \sin(\alpha + \theta) \frac{d\alpha}{ddis_{pro}} - m \sin \alpha \cos(\alpha + \theta) \frac{d\alpha}{ddis_{pro}}}{\sin^2(\alpha + \theta)}, \quad (36)$$

$$\frac{d\alpha}{ddis_{pro}} = \frac{\sin^2(\alpha + \theta)}{m \sin \theta}. \quad (37)$$

Final Expression for $dis'_{ref}(dis_{pro})$. Using Eqs. (34) and (37), we obtain the analytical form of $dis'_{ref}(dis_{pro})$, that is

$$\begin{aligned} dis'_{ref}(dis_{pro}) &= \frac{ddis_{ref}}{ddis_{pro}} \\ &= \frac{ddis_{ref}}{d\alpha} \frac{d\alpha}{ddis_{pro}} \\ &= \frac{t \sin \beta \sin^2(\alpha + \theta)}{m \sin \theta \sin^2(\alpha + \beta)}. \end{aligned} \quad (38)$$

Note that the side lengths in Fig. 9 (a) (e.g., t , m) can be derived from the known point coordinates and camera poses. The angles α , β , and θ can then be calculated using the law of cosines.

9. Implementation Details

We implement our method using PyTorch 2.0.0 on an RTX 3090. We conduct 30k iterations for training on the LLFF dataset, 10k iterations for DTU and MipNeRF-360 Datasets, and 4k iterations for Blender dataset. During training, the learning rate for scale was set to 0.03 across the LLFF, MipNeRF-360, and Blender datasets, while the other parameters remain consistent with those used in 3DGS.

	Setting	PSNR \uparrow	SSIM \uparrow	LPIPS \downarrow
3DGS		17.65	0.816	0.146
Ours	A. Average	18.92	0.836	0.128
	B. Nearest	19.57	0.860	0.108
	C. Weighted	19.05	0.850	0.119
	D. FRDB	19.76	0.864	0.109
	E. Average + FFDP	18.72	0.830	0.135
	F. Nearest + FFDP	19.74	0.860	0.108
	G. Weighted + FFDP	19.05	0.853	0.116
	H. FRDB + FFDP	20.21	0.869	0.102

Table 5. Ablation study on DTU with 3 input views.

9.1. Dataset Split

LLFF&MipNeRF-360. Following previous methods [25, 51], we sample images at intervals of 8 from the LLFF [22] and MipNeRF-360 [2] datasets to create the test set, while the remaining images are used as the training set. For the sparse-view synthesis task, we perform uniform sampling within the training set to select the training views. Consistent with previous work, we downsample all images by a factor of 8.

DTU. Following previous methods [45], we select 15 scenes from the DTU [16] dataset out of 124, specifically scene IDs 8, 21, 30, 31, 34, 38, 40, 41, 45, 55, 63, 82, 103, 110, and 114. For each scene, views 25, 22, and 28 are used as the 3-view training set, while views 1, 2, 9, 10, 11, 12, 14, 15, 23, 24, 26, 27, 29, 30, 31, 32, 33, 34, 35, 41, 42, 43, 45, 46, and 47 are designated as the test set. All images are downsampled by a factor of 4.

Blender. In the Blender [23] dataset, following previous methods [15], we select views 26, 86, 2, 55, 75, 93, 16, 73, and 8 for training. For evaluation, we uniformly sample 25 images from the test set. All images are downsampled by a factor of 2.

9.2. Additional Training Details

During training, we maintain most parameters consistent with those used in 3DGS. Here, we provide additional details beyond those in the main paper. Specifically, the threshold ϵ_d used in Flow-Filtered Depth Pruning is set to 1.0 for LLFF and DTU, 0.1 for MipNeRF-360, and 0.01 for Blender. The hyperparameter λ_c in the objective function was fixed at 0.2. Camera poses are estimated using COLMAP [32], following the methodology of existing sparse-view synthesis studies [20, 42, 51]. We utilize FlowFormer++ [34] as the optical flow estimator.

10. Extended Ablation Analysis

10.1. Quantitative Ablation Study on DTU Dataset

To complement the ablation results presented in the main paper for the LLFF real-world benchmark, we conduct additional experiments on the object-centric DTU dataset, with the results summarized in Tab. 5. Our Flow-Resilient Depth Blending (FRDB) method significantly improves sparse view synthesis performance over variants with alternative blending strategies. Furthermore, when combined with Flow-Filtered Depth Pruning (FFDP), our approach generally outperforms most configurations. This improvement is driven by cleaner, more accurate, and more comprehensive

Method	Point Number	PSNR \uparrow	SSIM \uparrow	LPIPS \downarrow
DNGaussian	43K	18.86	0.598	0.297
DNGaussian*	77K	19.96	0.684	0.232
CoR-GS	80K	20.29	0.705	0.201
FSGS	299K	20.34	0.695	0.207
Threshold	Point Number	PSNR \uparrow	SSIM \uparrow	LPIPS \downarrow
0.01	110K	20.21	0.678	0.218
0.1	191K	20.70	0.716	0.193
1.0	427K	21.07	0.738	0.177
2.0	456K	20.97	0.733	0.179
3.0	465K	20.89	0.733	0.180
4.0	469K	20.86	0.733	0.180

Table 6. Influence of distance threshold choices and point cloud comparison with state-of-the-art 3DGS-based competitors on the LLFF dataset with 3 input views. * denotes fused stereo initial point clouds.

Model Type	chairs	kitti	sintel	things_288960	things
PSNR \uparrow	21.049	21.060	21.045	21.068	21.075
SSIM \uparrow	0.738	0.738	0.738	0.739	0.738
LPIPS \downarrow	0.178	0.178	0.178	0.177	0.177

Table 7. The influence of different pre-trained flow estimation models on the LLFF dataset with 3 input views.

point clouds generated using epipolar depth priors, which lead to enhanced geometric precision and higher-quality details. However, under the Average settings (A. vs. E.), where depth estimates are extremely inaccurate, excessive splitting and replication of erroneous points during refinement lead to performance degradation. By contrast, in scenarios with relatively accurate depth priors, FFDP effectively enhances reconstruction quality by refining point clouds and preserving finer details. These consistent performance gains across different datasets demonstrate the robustness and effectiveness of our proposed method.

10.2. Influence of Distance Threshold

We further investigate the impact of varying threshold ϵ_d in FFDP, as detailed in Tab. 6. The table presents both quantitative metrics and the number of points in the Gaussian representation point cloud. Unlike Tab. 1 in the main paper, where competing methods’ results are taken from their original publications, we obtain these metrics by training their official implementations with default settings, as the point counts were not reported.

Examining the lower half of Tab. 6, we observe that when ϵ_d is set to low values (e.g., 0.1 or 0.01), the performance of NexusGS declines due to the insufficient number of points in the initial point clouds. This reduction in point density leads to excessive splitting in 3DGS, which introduces randomness in point placement. Moreover, the lack of supervision from sparse views prevents the generation of a dense, comprehensive point cloud, ultimately degrading performance.

The optimal results are achieved with a threshold of 1.0. As the threshold increases, more comprehensive and still relatively accurate initial points are obtained, significantly improving the quality of the generated point cloud and the final reconstruction. How-

Method	2 Views			3 Views			4 Views		
	PSNR \uparrow	SSIM \uparrow	LPIPS \downarrow	PSNR \uparrow	SSIM \uparrow	LPIPS \downarrow	PSNR \uparrow	SSIM \uparrow	LPIPS \downarrow
RegNeRF	16.16	0.396	0.455	19.08	0.587	0.336	20.95	0.689	0.272
FreeNeRF	17.12	0.490	0.364	19.63	0.612	0.308	21.63	0.709	0.253
SparseNeRF	17.51	0.450	0.423	19.86	0.624	0.328	21.09	0.681	0.295
3DGS	12.21	0.282	0.501	18.54	0.588	0.272	16.98	0.563	0.313
DNGaussian	15.92	0.454	0.391	19.12	0.591	0.294	20.58	0.688	0.253
FSGS	16.09	0.438	0.384	20.43	0.682	0.248	21.93	0.760	0.167
CoR-GS	14.63	0.417	0.423	20.45	0.712	0.196	21.62	0.761	0.163
Ours	19.28	0.659	0.220	21.07	0.738	0.177	22.12	0.774	0.158

Table 8. Quantitative evaluation of the impact of training views on the LLFF dataset.

ever, further increases may introduce additional inaccurate points, negatively affecting performance. Despite this, we find that as the threshold grows beyond 1.0, the impact on PSNR becomes more noticeable, while SSIM and LPIPS—metrics that align better with human visual perception—remain less affected. This suggests that our method exhibits tolerance for erroneous initial points, maintaining stable performance while revealing rich high-frequency details in the output.

We also quantitatively analyze the quality of the point clouds generated by state-of-the-art methods such as DNGaussian, FSGS, and CoR-GS, as shown in the upper half of Tab. 6. Regardless of whether random or fused stereo initial point clouds (indicated by an asterisk) are used, DNGaussian, as a lightweight design-focused method, consistently generates fewer points and provides less comprehensive coverage than our approach, even at $\epsilon_d = 0.01$, resulting in inferior performance. Although FSGS generates more points, its limited point addition strategy results in lower accuracy and coverage. Notably, even with a reduced number of points (e.g., $\epsilon_d = 0.1$), our method still outperforms FSGS. As for CoR-GS, while it generates relatively comprehensive coverage, it lacks the ability to produce a dense point cloud. This limitation is reflected in the point count, ultimately restricting the reconstruction quality, especially in high-frequency details. In contrast, NexusGS, with epipolar depth priors, generates a more accurate, dense, and comprehensive point cloud, leading to superior reconstruction performance.

10.3. Robustness Across Various Flow Estimators

Inspired by existing approaches [20, 51], which utilize monocular depth estimators to provide depth priors, we hypothesize that similar variability in performance might occur when using different optical flow estimators with varying network parameters. To explore this possibility, we conduct experiments on the LLFF dataset, comparing the performance of our method using optical flow estimators trained on five different datasets. Specifically, we evaluate the *chairs*, *kitti*, *sintel*, *things_288960*, and *things* models of FlowFormer++. The quantitative results are summarized in Tab. 7. As illustrated, despite utilizing different pretrained flow estimation models, our method consistently shows minimal variations in PSNR, with SSIM and LPIPS scores remaining nearly identical across the different models. These results highlight the robustness of our approach, demonstrating its effectiveness regardless of the

specific optical flow estimator employed.

10.4. Robustness on Varying View Counts

To validate the robustness of our method under varying numbers of training views, we conduct experiments on the LLFF dataset, with results presented in Tab. 8. Our method consistently outperforms all competitors when using 2, 3, and 4 views. Notably, with only 2 training views, COLMAP fails to generate a fused stereo point cloud, leading to poor performance by DNGaussian, FSGS, and CoR-GS, which perform even worse than NeRF-based methods. In contrast, our method does not suffer from this limitation. By leveraging the point cloud generated through our approach, we achieve superior results with just 2 views, effectively overcoming the constraints of previous 3DGS methods and surpassing NeRF-based methods across all evaluated metrics.

11. Additional Visual Results

Additional visual results are provided in the supplementary materials. Specifically, Fig. 10 showcases the results of our method on the Blender dataset. As shown, our method achieves a more complete and detailed reconstruction compared to previous approaches. This improvement is attributed to the accurate geometry provided by the precise point cloud, which enables the faithful reconstruction of finer textures.

We also present additional visual results on the DTU dataset in Fig. 11. It is evident that the results from NeRF-based methods, constrained by depth priors, are adversely affected by floaters, leading to degraded reconstruction quality. This suggests that their depth priors are not well-suited for object-centered datasets. In contrast, subsequent 3DGS-based methods that utilize depth priors mitigate the presence of floaters. However, due to the lack of dense and accurate point clouds, their final reconstructions appear visually smoother, lacking finer detail.

Furthermore, Figs. 12 and 13 present the results for each test scene on the LLFF and DTU datasets, respectively. Fig. 14 compares the depth maps of our method and the competitors.

12. Discussion, Limitations, and Future Work

Despite NexusGS’s remarkable performance and generalizability, it, like most sparse-view synthesis methods, relies on known camera

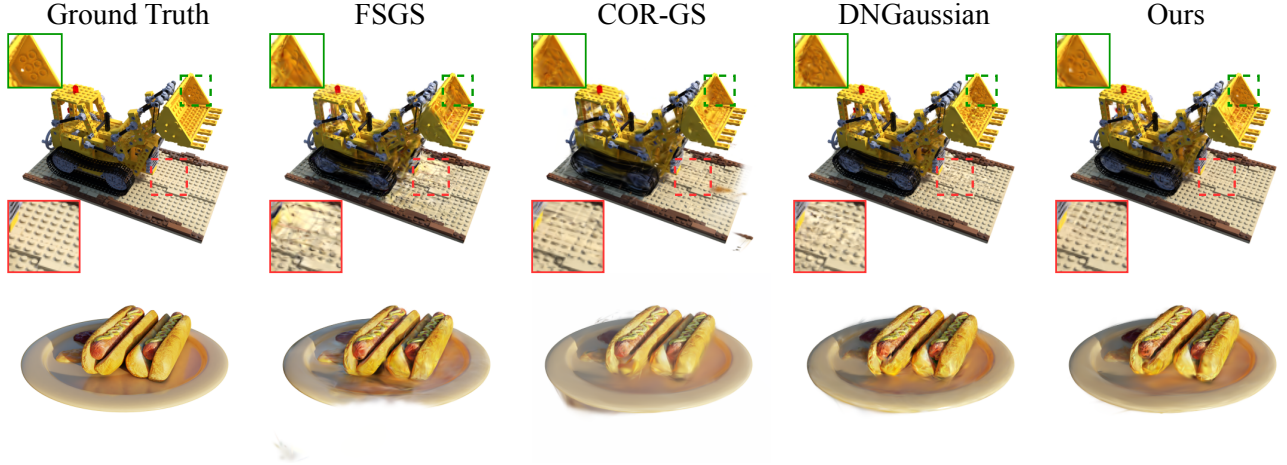


Figure 10. Visual results on the Blender dataset with 8 input views.

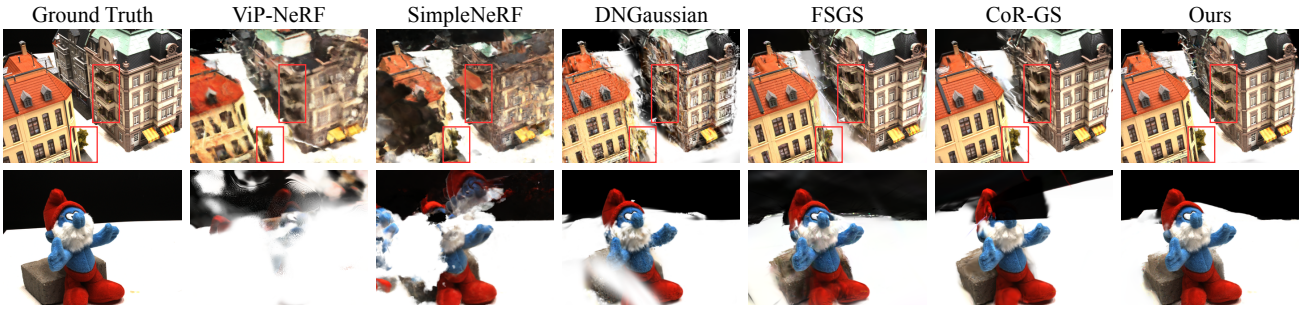


Figure 11. Additional visual comparisons on the DTU dataset with 3 input views.

Perturbation	0	0.02	0.04	0.06	0.08	0.1
DNGaussian	0.591	0.586	0.565	0.556	0.540	0.476
FSGS	0.682	0.688	0.664	0.633	0.606	0.579
CoR-GS	0.712	0.693	0.664	0.639	0.609	0.586
Ours	0.738	0.724	0.690	0.653	0.617	0.588

Table 9. Sensitivity analysis of calibration errors on the LLFF dataset with 3 input views using SSIM.

poses to enforce epipolar constraints. To evaluate the robustness of our method, we conduct a sensitivity analysis of camera calibration errors, using the SSIM score as the primary metric, as summarized in Tab. 9. Perturbations are introduced to the camera pose along all axes, resulting in performance degradation across all competitors, all of which depend on accurate pose information. Severe overfitting is observed when perturbations reach 0.1. In contrast, our method demonstrates superior robustness, consistently outperforming others despite pose errors, thanks to our effective error-handling strategies, FRDB and FFDP.

Although recent pose-free methods, such as COGS [17], bypass the need for camera poses, the trade-off between flexibility and rendering accuracy leaves room for improvement, offering a promising avenue for future work.

References

- [1] Jonathan T Barron, Ben Mildenhall, Matthew Tancik, Peter Hedman, Ricardo Martin-Brualla, and Pratul P Srinivasan. Mip-nerf: A multiscale representation for anti-aliasing neural radiance fields. In *ICCV*, pages 5855–5864, 2021. 1, 2
- [2] Jonathan T Barron, Ben Mildenhall, Dor Verbin, Pratul P Srinivasan, and Peter Hedman. Mip-nerf 360: Unbounded anti-aliased neural radiance fields. In *CVPR*, pages 5470–5479, 2022. 1, 6, 11
- [3] Shariq Farooq Bhat, Reiner Birkel, Diana Wofk, Peter Wonka, and Matthias Müller. Zoedepth: Zero-shot transfer by combining relative and metric depth. *arXiv preprint arXiv:2302.12288*, 2023. 2
- [4] David Charatan, Sizhe Lester Li, Andrea Tagliasacchi, and Vincent Sitzmann. pixelsplat: 3d gaussian splats from image pairs for scalable generalizable 3d reconstruction. In *CVPR*, pages 19457–19467, 2024. 3
- [5] Anpei Chen, Zexiang Xu, Fuqiang Zhao, Xiaoshuai Zhang, Fanbo Xiang, Jingyi Yu, and Hao Su. Mvsnerf: Fast generalizable radiance field reconstruction from multi-view stereo. In *ICCV*, pages 14124–14133, 2021. 3
- [6] Tianlong Chen, Peihao Wang, Zhiwen Fan, and Zhangyang Wang. Aug-nerf: Training stronger neural radiance fields with triple-level physically-grounded augmentations. In *CVPR*,



Figure 12. Per-scene visual results on the LLFF dataset with 3 input views.

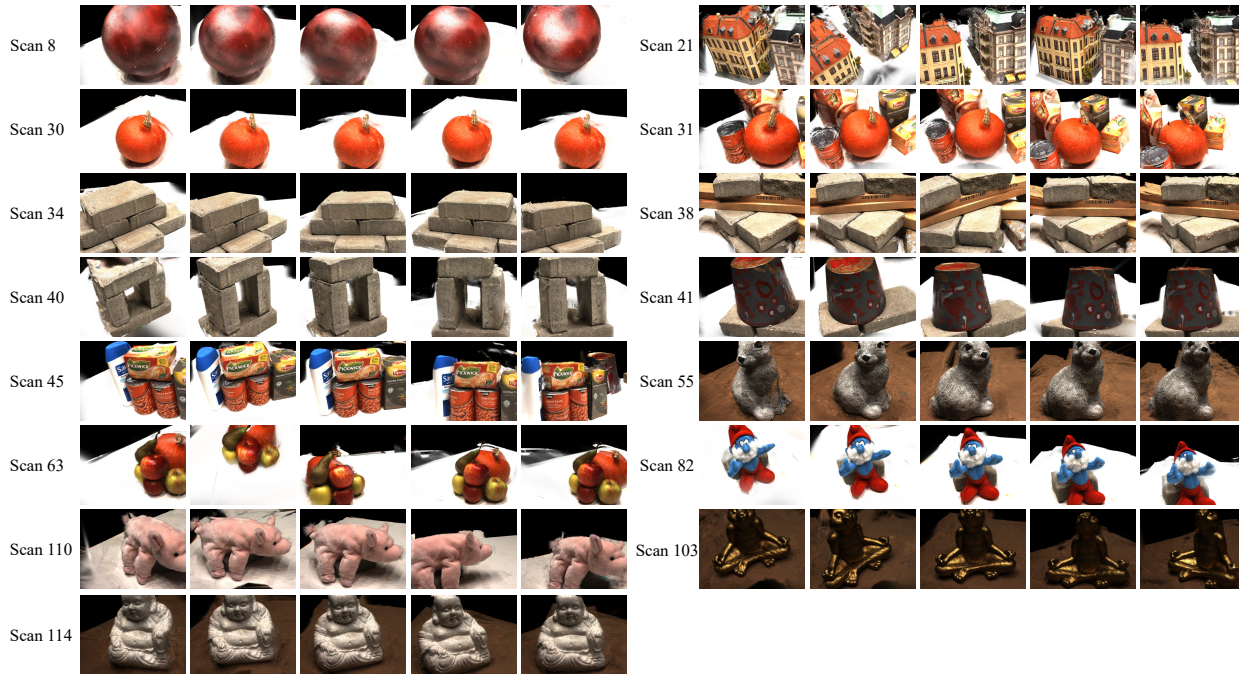


Figure 13. Per-scene visual results on the DTU dataset with 3 input views.

- pages 15191–15202, 2022. [2](#)
- [7] Kai Cheng, Xiaoxiao Long, Kaizhi Yang, Yao Yao, Wei Yin, Yuexin Ma, Wenping Wang, and Xuejin Chen. Gaussianpro: 3d gaussian splatting with progressive propagation. In *ICML*, 2024. [2](#)
- [8] Jaeyoung Chung, Jeongtaek Oh, and Kyoung Mu Lee. Depth-regularized optimization for 3d gaussian splatting in few-shot images. In *CVPR*, pages 811–820, 2024. [3](#)
- [9] Kangle Deng, Andrew Liu, Jun-Yan Zhu, and Deva Ramanan. Depth-supervised nerf: Fewer views and faster training for free. In *CVPR*, pages 12882–12891, 2022. [3](#), [6](#)
- [10] Kyle Gao, Yina Gao, Hongjie He, Dening Lu, Linlin Xu, and Jonathan Li. Nerf: Neural radiance field in 3d vision, a comprehensive review. *arXiv preprint arXiv:2210.00379*, 2022. [3](#)
- [11] Zelin Gao, Weichen Dai, and Yu Zhang. Hg3-nerf: Hier-

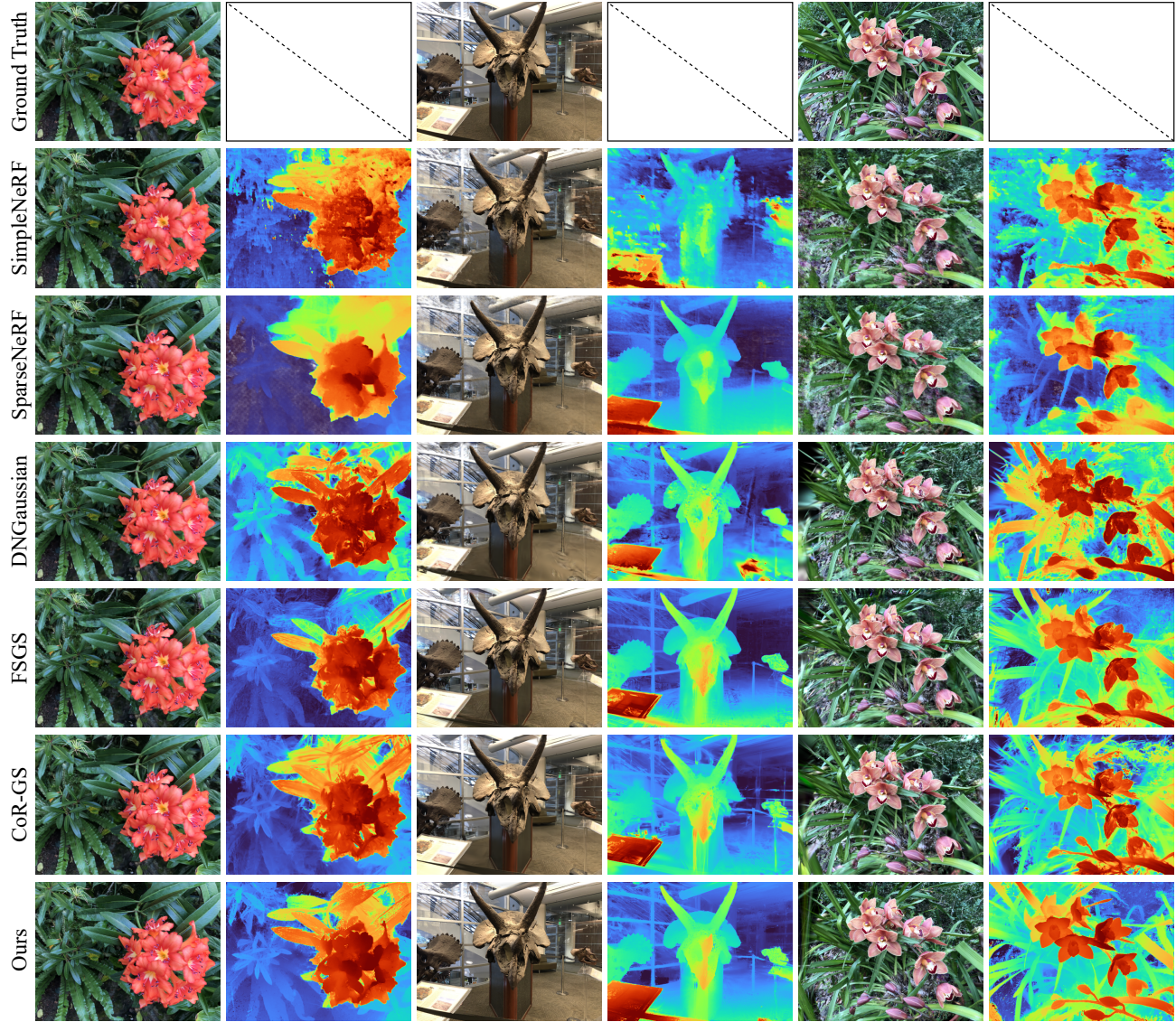


Figure 14. Visual comparisons of depth maps on the LLFF dataset with 3 input views.

- archical geometric, semantic, and photometric guided neural radiance fields for sparse view inputs. *arXiv preprint arXiv:2401.11711*, 2024. 3
- [12] Stephan J Garbin, Marek Kowalski, Matthew Johnson, Jamie Shotton, and Julien Valentin. Fastnerf: High-fidelity neural rendering at 200fps. In *ICCV*, pages 14346–14355, 2021. 2
- [13] Yuan-Chen Guo, Di Kang, Linchao Bao, Yu He, and Song-Hai Zhang. Nerfren: Neural radiance fields with reflections. In *CVPR*, pages 18409–18418, 2022. 2
- [14] Binbin Huang, Zehao Yu, Anpei Chen, Andreas Geiger, and Shenghua Gao. 2d gaussian splatting for geometrically accurate radiance fields. In *ACM SIGGRAPH*, pages 1–11, 2024. 2
- [15] Ajay Jain, Matthew Tancik, and Pieter Abbeel. Putting nerf on a diet: Semantically consistent few-shot view synthesis. In *ICCV*, pages 5885–5894, 2021. 3, 6, 7, 11
- [16] Rasmus Jensen, Anders Dahl, George Vogiatzis, Engin Tola, and Henrik Aanæs. Large scale multi-view stereopsis evaluation. In *CVPR*, pages 406–413, 2014. 6, 11
- [17] Kaiwen Jiang, Yang Fu, Yash Belhe, Xiaolong Wang, Hao Su, Ravi Ramamoorthi, et al. A construct-optimize approach to sparse view synthesis without camera pose. In *ACM SIGGRAPH*, 2024. 13
- [18] Mohammad Mahdi Johari, Yann Lepoittevin, and François Fleuret. Geonerf: Generalizing nerf with geometry priors. In *CVPR*, pages 18365–18375, 2022. 2
- [19] Bernhard Kerbl, Georgios Kopanas, Thomas Leimkühler, and George Drettakis. 3d gaussian splatting for real-time radiance field rendering. *ACM TOG*, 42(4):1–14, 2023. 1, 2, 3, 6, 7
- [20] Jiahe Li, Jiawei Zhang, Xiao Bai, Jin Zheng, Xin Ning, Jun

- Zhou, and Lin Gu. Dngaussian: Optimizing sparse-view 3d gaussian radiance fields with global-local depth normalization. In *CVPR*, 2024. 2, 6, 7, 8, 11, 12
- [21] Tianqi Liu, Guangcong Wang, Shoukang Hu, Liao Shen, Xinyi Ye, Yuhang Zang, Zhiguo Cao, Wei Li, and Ziwei Liu. Mvsgaussian: Fast generalizable gaussian splatting reconstruction from multi-view stereo. In *ECCV*, pages 37–53. Springer, 2024. 3
- [22] Ben Mildenhall, Pratul P Srinivasan, Rodrigo Ortiz-Cayon, Nima Khademi Kalantari, Ravi Ramamoorthi, Ren Ng, and Abhishek Kar. Local light field fusion: Practical view synthesis with prescriptive sampling guidelines. *ACM TOG*, 38(4):1–14, 2019. 6, 11
- [23] Ben Mildenhall, Pratul P Srinivasan, Matthew Tancik, Jonathan T Barron, Ravi Ramamoorthi, and Ren Ng. Nerf: Representing scenes as neural radiance fields for view synthesis. *Communications of the ACM*, 65(1):99–106, 2021. 1, 6, 7, 11
- [24] Thomas Müller, Alex Evans, Christoph Schied, and Alexander Keller. Instant neural graphics primitives with a multi-resolution hash encoding. *ACM TOG*, 41(4):1–15, 2022. 2
- [25] Michael Niemeyer, Jonathan T Barron, Ben Mildenhall, Mehdi SM Sajjadi, Andreas Geiger, and Noha Radwan. Regnerf: Regularizing neural radiance fields for view synthesis from sparse inputs. In *CVPR*, pages 5480–5490, 2022. 3, 6, 11
- [26] Avinash Paliwal, Wei Ye, Jinhui Xiong, Dmytro Kotovenko, Rakesh Ranjan, Vikas Chandra, and Nima Khademi Kalantari. Coherentgs: Sparse novel view synthesis with coherent 3d gaussians. In *ECCV*, pages 19–37. Springer, 2024. 3
- [27] Alec Radford, Jong Wook Kim, Chris Hallacy, Aditya Ramesh, Gabriel Goh, Sandhini Agarwal, Girish Sastry, Amanda Askell, Pamela Mishkin, Jack Clark, et al. Learning transferable visual models from natural language supervision. In *ICML*, pages 8748–8763, 2021. 3
- [28] René Ranftl, Alexey Bochkovskiy, and Vladlen Koltun. Vision transformers for dense prediction. In *ICCV*, pages 12179–12188, 2021. 2
- [29] René Ranftl, Katrin Lasinger, David Hafner, Konrad Schindler, and Vladlen Koltun. Towards robust monocular depth estimation: Mixing datasets for zero-shot cross-dataset transfer. *IEEE TPAMI*, 44(3):1623–1637, 2020. 2
- [30] Christian Reiser, Songyou Peng, Yiyi Liao, and Andreas Geiger. Kilonerf: Speeding up neural radiance fields with thousands of tiny mlps. In *ICCV*, pages 14335–14345, 2021. 2
- [31] Barbara Roessle, Jonathan T Barron, Ben Mildenhall, Pratul P Srinivasan, and Matthias Nießner. Dense depth priors for neural radiance fields from sparse input views. In *CVPR*, pages 12892–12901, 2022. 3
- [32] Johannes L Schonberger and Jan-Michael Frahm. Structure-from-motion revisited. In *CVPR*, pages 4104–4113, 2016. 2, 11
- [33] Ruoxi Shi, Xinyue Wei, Cheng Wang, and Hao Su. Zerorf: fast sparse view 360 reconstruction with zero pretraining. In *CVPR*, pages 21114–21124, 2024. 3
- [34] Xiaoyu Shi, Zhaoyang Huang, Dasong Li, Manyuan Zhang, Ka Chun Cheung, Simon See, Hongwei Qin, Jifeng Dai, and Hongsheng Li. Flowformer++: Masked cost volume autoencoding for pretraining optical flow estimation. In *CVPR*, pages 1599–1610, 2023. 4, 11
- [35] Nagabhushan Somraj, Sai Harsha Mupparaju, Adithyan Karanayil, and Rajiv Soundararajan. Simple-rf: Regularizing sparse input radiance fields with simpler solutions. *arXiv preprint arXiv:2404.19015*, 2024. 3, 6
- [36] Nagabhushan Somraj and Rajiv Soundararajan. Vip-nerf: Visibility prior for sparse input neural radiance fields. In *ACM SIGGRAPH*, pages 1–11, 2023. 3, 6
- [37] Mohammed Suhail, Carlos Esteves, Leonid Sigal, and Ameesh Makadia. Light field neural rendering. In *CVPR*, pages 8269–8279, 2022. 2
- [38] Cheng Sun, Min Sun, and Hwann-Tzong Chen. Direct voxel grid optimization: Super-fast convergence for radiance fields reconstruction. In *CVPR*, pages 5459–5469, 2022. 1, 2
- [39] Mukund Varma T, Peihao Wang, Xuxi Chen, Tianlong Chen, Subhashini Venugopalan, and Zhangyang Wang. Is attention all that NeRF needs? In *ICLR*, 2023. 2
- [40] Mikaela Angelina Uy, Ricardo Martin-Brualla, Leonidas Guibas, and Ke Li. Scade: Nerfs from space carving with ambiguity-aware depth estimates. In *CVPR*, pages 16518–16527, 2023. 3
- [41] Dor Verbin, Peter Hedman, Ben Mildenhall, Todd Zickler, Jonathan T Barron, and Pratul P Srinivasan. Ref-nerf: Structured view-dependent appearance for neural radiance fields. In *CVPR*, pages 5481–5490, 2022. 2
- [42] Guangcong Wang, Zhaoxi Chen, Chen Change Loy, and Ziwei Liu. Sparsenerf: Distilling depth ranking for few-shot novel view synthesis. In *ICCV*, pages 9065–9076, 2023. 1, 2, 6, 7, 8, 11
- [43] Qianqian Wang, Zhicheng Wang, Kyle Genova, Pratul P Srinivasan, Howard Zhou, Jonathan T Barron, Ricardo Martin-Brualla, Noah Snavely, and Thomas Funkhouser. Ibrnet: Learning multi-view image-based rendering. In *CVPR*, pages 4690–4699, 2021. 2
- [44] Qiangeng Xu, Zexiang Xu, Julien Philip, Sai Bi, Zhixin Shu, Kalyan Sunkavalli, and Ulrich Neumann. Point-nerf: Point-based neural radiance fields. In *CVPR*, pages 5438–5448, 2022. 2
- [45] Jiawei Yang, Marco Pavone, and Yue Wang. Freenerf: Improving few-shot neural rendering with free frequency regularization. In *CVPR*, pages 8254–8263, 2023. 1, 3, 6, 7, 11
- [46] Alex Yu, Ruilong Li, Matthew Tancik, Hao Li, Ren Ng, and Angjoo Kanazawa. Plenotrees for real-time rendering of neural radiance fields. In *ICCV*, pages 5752–5761, 2021. 1
- [47] Alex Yu, Vickie Ye, Matthew Tancik, and Angjoo Kanazawa. pixelnerf: Neural radiance fields from one or few images. In *CVPR*, pages 4578–4587, 2021. 2, 3
- [48] Zehao Yu, Anpei Chen, Binbin Huang, Torsten Sattler, and Andreas Geiger. Mip-splatting: Alias-free 3d gaussian splatting. In *CVPR*, pages 19447–19456, 2024. 2
- [49] Jiawei Zhang, Jiahe Li, Xiaohan Yu, Lei Huang, Lin Gu, Jin Zheng, and Xiao Bai. Cor-gs: Sparse-view 3d gaussian splatting via co-regularization. In *ECCV*, 2024. 3, 6, 7, 8
- [50] Hanxin Zhu, Tianyu He, Xin Li, Bingchen Li, and Zhibo Chen. Is vanilla mlp in neural radiance field enough for few-shot view synthesis? In *CVPR*, pages 20288–20298, 2024.

- [51] Zehao Zhu, Zhiwen Fan, Yifan Jiang, and Zhangyang Wang. Fsgs: Real-time few-shot view synthesis using gaussian splatting. In *ECCV*, 2024. [2](#), [3](#), [6](#), [7](#), [8](#), [11](#), [12](#)